Report

Current Biology

Rho GTPase dynamics distinguish between models of cortical excitability

Highlights

- Accumulation of active Rho precedes accumulation of total Rho in cortical waves
- An activator-inhibitor model predicts Rho activation peaks before total Rho
- An activator-depleted substrate model predicts total Rho peaks before active Rho
- The results support the activator-inhibitor model

Authors

Dominic Chomchai, Marcin Leda, Adriana Golding, George von Dassow, William M. Bement, Andrew B. Goryachev

Correspondence

dassow@uoregon.edu (G.v.D.), wmbement@wisc.edu (W.M.B.), andrew.goryachev@ed.ac.uk (A.B.G.)

In brief

Cortical excitability is the ability of the cell cortex to generate pulses and waves of Rho GTPase activity. Using live-cell imaging and theoretical modeling, Chomchai, Leda et al. show that cortical excitability is best explained by a model in which Rho GTPase pulses and waves arise from GTPase autoactivation coupled to delayed autoinhibition.

Chomchai et al., 2025, Current Biology *35*, 1414–1421
March 24, 2025
https://doi.org/10.1016/j.cub.2025.02.003

CellPress

CellPress

Current Biology

Report

Rho GTPase dynamics distinguish between models of cortical excitability

Dominic Chomchai,[1,2,3,7] Marcin Leda,[4,7] Adriana Golding,[1,5] George von Dassow,[6,8,*] William M. Bement,[1,2,3,8,9,*] and Andrew B. Goryachev[4,8,*]

[1]Graduate Program in Cellular and Molecular Biology, University of Wisconsin-Madison, 250 N Mills St, Madison, WI 53706, USA
[2]Center for Quantitative Imaging, University of Wisconsin-Madison, 250 N Mills St, Madison, WI 53706, USA
[3]Department of Integrative Biology, University of Wisconsin-Madison, 250 N Mills St, Madison, WI 53706, USA
[4]Centre for Engineering Biology, School of Biological Sciences, University of Edinburgh, C.H. Waddington Building, Max Born Crescent, EH9 3BF Edinburgh, UK
[5]Neurosciences and Cellular and Structural Biology Division, Eunice Kennedy Shriver National Institute of Child Health and Human Development, National Institutes of Health, 1 Center Dr, Bethesda, MD 20892, USA
[6]Oregon Institute of Marine Biology, 63466 Boat Basin Road, Charleston, OR 97420, USA
[7]These authors contributed equally
[8]These authors contributed equally
[9]Lead contact
*Correspondence: dassow@uoregon.edu (G.v.D.), wmbement@wisc.edu (W.M.B.), andrew.goryachev@ed.ac.uk (A.B.G.)
https://doi.org/10.1016/j.cub.2025.02.003

SUMMARY

The Rho GTPases pattern the cell cortex in a variety of fundamental cell-morphogenetic processes, including division, wound repair, and locomotion. It has recently become apparent that this patterning arises from the ability of the Rho GTPases to self-organize into static and migrating spots, contractile pulses, and propagating waves in cells from yeasts to mammals.[1] These self-organizing Rho GTPase patterns have been explained by a variety of theoretical models that require multiple interacting positive and negative feedback loops. However, it is often difficult, if not impossible, to discriminate between different models simply because the available experimental data do not simultaneously capture the dynamics of multiple molecular concentrations and biomechanical variables at fine spatial and temporal resolution. Specifically, most studies typically provide either the total Rho GTPase signal or the Rho GTPase activity, as reported by various sensors, but not both. Therefore, it remains largely unknown how membrane accumulation of Rho GTPases (i.e., Rho membrane enrichment) is related to Rho activity. Here, we dissect the dynamics of RhoA by simultaneously imaging both total RhoA and active RhoA in propagating waves of Rho activity and F-actin polymerization.[2–5] We find that within nascent waves, accumulation of active RhoA precedes that of total RhoA, and we exploit this finding to distinguish between two popular theoretical models previously used to explain propagating cortical Rho waves.

RESULTS AND DISCUSSION

Rho GTPase activity rise precedes accumulation of total Rho in waves

In many fundamental cellular[3,4,6–10] and developmental[11,12] processes, Rho GTPases are deployed as periodic pulses or propagating waves of activity that are collectively referred to as "cortical excitability."[2] To provide a detailed analysis of spatiotemporal dynamics of RhoA in cortical excitability, we amplified cytokinetic waves in starfish oocytes undergoing meiosis via ectopic expression of the cytokinetic Rho guanine nucleotide exchange factor (GEF) Ect2[3] or induced such waves in immature frog oocytes via ectopic expression of Ect2 and the cytokinetic Rho GTPase-activating protein (GAP) RGA-3/4.[4] Such waves mimic those in the cytokinetic apparatus[6] but have the virtue of continuing for many minutes or hours and encompassing the majority, if not the entirety, of the cell cortex, permitting a detailed record of their behavior to be captured. In contrast, the furrow waves are normally restricted to anaphase and quickly become inaccessible to high-resolution imaging as the furrow ingresses. As a result, amplified and induced waves have been used to probe the network dynamics of cytokinetic Rho GTPase signaling,[3,13] wiring of the underlying signaling networks,[4] and relationships between cell shape, wave propagation, and signaling hierarchies.[14,15] More broadly, propagating waves offer distinct advantages over other cortical states that lack the dynamicity of waves. First, waves present as readily distinguishable alternating maxima and minima of fluorescence intensity moving in a periodic pattern. Thus, standard image analysis methods can be readily applied to extract wave velocity, spatial wavelength, and temporal period. These constitute a quantitative signature of the wave pattern, which can be compared with proposed theoretical models.[4,16] Second, because wave propagation consists of periodically repeating cycles of biochemical reactions and molecule translocations between the plasma membrane and the cytoplasm, time series of

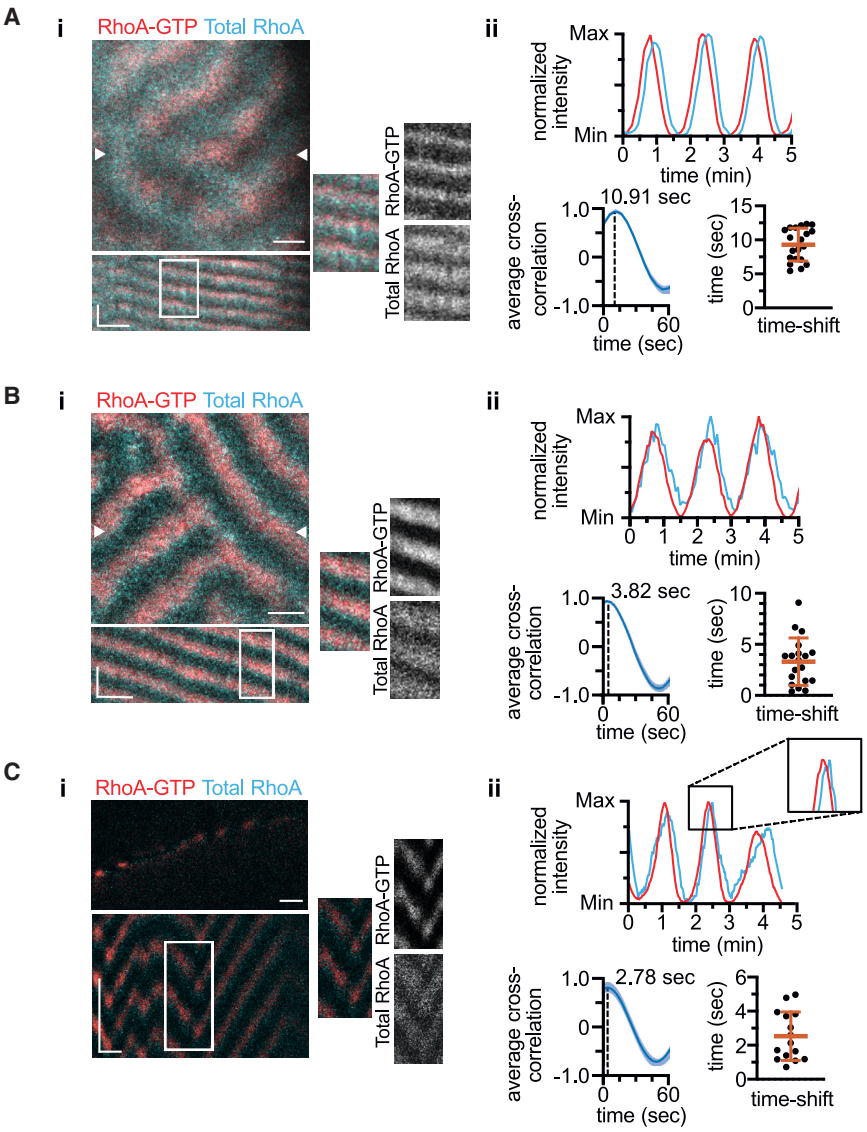

Figure 1. RhoA activity leads RhoA membrane enrichment in starfish and frog oocyte cortical excitability

(A–C) (i) Representative still images and corresponding kymographs of RhoA-GTP (red) and total RhoA (cyan) waves from a starfish oocyte *en face* video (A), a frog immature oocyte *en face* video (B), and a frog immature oocyte medial section difference video (C). See also Videos S1, S2, and S3. (ii) Quantification for the corresponding videos in (A)–(C). Top: representative normalized quantitative wave profiles of RhoA-GTP (red) and total RhoA (cyan) waves from the corresponding video in (A)–(C) demonstrate that RhoA-GTP leads total Rho enrichment. Bottom left: average cross-correlation of the corresponding videos in (A)–(C). Shaded area: standard deviation (SD). Vertical dashed line: mean time shift between the RhoA-GTP/total RhoA signals. (A: 10.91 ± 0.69 s; B: 3.82 ± 1.10 s; C: 4.99 ± 2.86 s; ±SD). Bottom right: overall mean time shift between RhoA-GTP and total RhoA signals. Each point represents the time shift measurement of an individual cell under the same conditions as (A)–(C) (A: 9.30 ± 2.41 s, $n = 20$; B: 3.30 ± 2.32 s, $n = 19$; C: 2.53 ± 1.4 s, $n = 15$; ±SD; p value < 0.0001 for each; two-tailed one-sample t-test).

Horizontal scale bars: 10 μm. Vertical scale bars: 2 min. Arrowheads indicate the location used for kymograph generation.

See also Figures S1 and S2.

fluorescence signals carry valuable mechanistic information. For example, they reveal the temporal sequence of various processes, which may suggest causal relationships between them. Such data inform the construction of plausible mechanistic models. Further, specific time delays, measured, for example, between the concentration maxima of the key molecular players, provide information necessary to quantitatively constrain the values of parameters to be associated with the model interactions.

Because the membrane-bound pool of RhoA consists of dynamically interconverting active and inactive GTPase states, two independent fluorescence signals representative of the total RhoA and active, GTP-bound RhoA are required for the complete characterization of RhoA dynamics at the cell cortex. To visualize total RhoA, we employed previously characterized, internally tagged frog RhoA[17] (IT-RhoA) and developed the equivalent echinoderm version for starfish. Both probes localize to the cytokinetic furrow[17] (Figure S1A) and their furrow localization is amplified by co-expression of Ect2 (data not shown). The merits of internal fluorescent protein tagging of Rho GTPases have been pointed out previously for both yeast[18–20] and vertebrates.[1,17,21] To visualize RhoA-GTP, we employed mCherry-rGBD, which has been used previously in both starfish and frog to track active RhoA.[3,15,22,23] Starfish IT-RhoA produced a robust fluorescence signal in Ect2-amplified waves in starfish oocytes (Figure S1B). Interestingly, direct comparison revealed that IT-RhoA waves follow RhoA-GTP waves with a delay, which is evident in *en face* videos, still images, and kymographs as a color shift (Figure 1Ai, Video S1). This delay is also evident from intensity plots of the raw data (Figure S1C). To quantify the delay, wave amplitude was normalized to lie between 0 (minimum) and 1 (maximum), which allows for more precise quantification of phase differences against a background of data variability (see STAR Methods). (We emphasize that normalized plots do not preserve the relationship between the absolute levels, as active RhoA always represents some fraction of the total RhoA). Correlation analysis of the normalized data from a representative cell showed that IT-RhoA waves followed RhoA-GTP waves with a 10.91 ± 0.69 s delay (Figure 1Aii). Quantification of the normalized data from multiple cells revealed an average of 9.3 ± 2.4 s ($n = 20$ cells from 3 experiments; Figure 1Aii), corresponding to an oscillation phase shift of 9.5% (period = 97 ± 18.7 s).

In frog, IT-RhoA produced a robust fluorescence signal in induced waves (Figure S1D). However, the difference between

IT-RhoA and RhoA-GTP signals, although still detectable in *en face* videos, their kymographs, and the normalized time series (Figure 1B; Video S2), was smaller than in starfish, with a shift of 3.82 ± 1.10 s in a representative cell and an average shift of 3.30 ± 2.32 s (n = 19 cells from 5 experiments). Because this shift was less than the interval of image acquisition, we adopted single optical plane imaging in a medial section (Figure 1Ci, Video S3), which shortened the sampling interval from ∼4 to ∼1 s. Consistent with the *en face* analysis, this revealed a small but significant delay of 2.78 ± 1.41 s from a representative cell and an average of 2.53 ± 1.40 s (n = 15 cells from 4 experiments, Figures 1Cii and S1E). This constitutes only a 3.6% oscillation phase shift (period = 70 ± 17.0 s). To determine whether the delay was specific to the acute wave regime, we also conducted experiments in which RGA-3/4 was reduced or eliminated. Consistent with previous results,[4] reducing the RGA-3/4 concentration resulted in a significant increase in the wave period (Figures S2A and S2B), whereas elimination of RGA-3/4 altogether resulted in low amplitude pulses (Figure S2C). Nonetheless, under both conditions, the shift between active and total Rho remained (Figures S2A–S2E). Finally, to ensure that the shift did not reflect fluorophore choices, the behavior of mCherry-IT-RhoA (mCh-IT-RhoA) was compared with GFP-rGBD in oocytes exhibiting waves. Although the mCh-IT-RhoA signal was noticeably weaker than that of the GFP-IT-RhoA (compare Figure 1C to S2F), a small but significant delay was nonetheless evident between the peaks of GFP-rGBD and mCh-IT-RhoA (Figure S2G). Moreover, we note that there must be some inherent delay between the activation of RhoA and binding of the rGBD probe to the active RhoA, implying that the measurements actually underestimate the delay between the active and total RhoA.

Importantly, these results clearly demonstrate that the waves of Rho GTPase activity reported by us and others in the oocytes and embryos of frogs[3,4] and echinoderms[3,4,15,24] are not simply waves of local GTPase activation-inactivation against a background of constant total plasma-membrane-associated GTPase. Rather, they show for the first time that the waves comprise changes in both RhoA activity and total plasma membrane RhoA levels. Further, the delay between the peaks of RhoA activity and total RhoA unambiguously indicates that the change in GTPase activity precedes the change in its total quantity, thus suggesting a causal relationship between the two.

Testing theoretical models of RhoA wave generation

We next asked whether our experimental results could shed additional light on the molecular mechanisms of Rho GTPase dynamics and, consequently, wave generation. Two distinct types of mechanistically minimal two-variable models—activator-inhibitor and activator-depleted substrate (ADS)—have been extensively used to explain propagation of waves in biological systems.[25,26] Both models assume positive feedback in which the activator stimulates its own activation or production but they differ in how their negative feedback is implemented: in activator-inhibitor models, negative feedback arises from an inhibitor whose accumulation or activity is stimulated by the activator. As a result, the activator is "chased" by a wave of the inhibitor. In ADS models, negative feedback arises from the consumption of some substrate essential for the activator production. As a result, the wave of activator is chased by a wave of depletion of the substrate in question. In the specific context of pattern formation by Rho GTPases, RhoA-GTP is the activator and engages in positive feedback by directly or indirectly stimulating a Rho GEF.[1,27,28] In activator-inhibitor models for the GTPases, the inhibitor is surmised to be a GAP that is a downstream target of the active GTPase.[1] The activator-inhibitor models are appealing, based on demonstrations of actin filaments serving as prototypical inhibitors in a number of systems,[3,7,11,29] at least in part based on their ability to associate with a Rho GAP.[4,7,11,30] Simply because active GTPase is generated from inactive GTPase, RhoA-GTP and RhoA-GDP satisfy the conditions for being the activator and the essential substrate subject to depletion. Therefore, the ADS models for the Rho GTPases are appealing because they have the potential to apply to any GTPase that undergoes nucleotide cycling. The ADS models accounting for the RhoA membrane-cytoplasmic shuttling and nucleotide cycling (Figure 2A) were first developed to explain spontaneous formation of the stationary spots or clusters of GTPase activity in cell migration and cell polarity.[1,31–34]

However, the core ADS model defined as shown in Figure 2A cannot exhibit oscillatory or excitable dynamics (see analysis of the ADS+ model in STAR Methods). To alleviate this deficiency, a hypothetical reaction of GAP-mediated simultaneous inactivation and membrane detachment of active RhoA was suggested[15,35] (magenta arrow, Figure 2B). The thus-modified ADS model, referred to in the following as the ADS+ model to distinguish it from the parental model, exhibits oscillatory and excitable dynamics (see STAR Methods) yet remains a two-variable model.

A complete mathematical model of cellular dynamics of RhoA must include at minimum two independent variables that account for the existence of two forms of RhoA, which are interconverted on the membrane by the enzyme-catalyzed reactions of the nucleotide cycle.[36,37] A natural choice of these variables are RT, which represents the local membrane concentration of the active form, RhoA-GTP, and RD, which represents the membrane concentration of the inactive form, RhoA-GDP. However, RhoA-GDP cannot be directly assayed, while the total concentration of membrane-bound Rho is reported by the signal of the IT-RhoA. It is thus convenient to replace RD with the total concentration of membrane-bound Rho, TR, which is simply the sum of RT and RD. Then, any model describing the dynamics of RhoA in terms of RT and RD can be readily recast into RT and TR (see STAR Methods), whose dynamics are directly comparable with the experimental data.

The prototypical two-variable activator-inhibitor model does not satisfy the above condition of completeness but can be extended to add the production of RhoA-GTP from RhoA-GDP as shown in Figure 2C, resulting in a three-variable activator-depleted substrate-inhibitor (ADSI) model.[3,4] This compound model consists of the ADS and the activator-inhibitor submodules linked by a common activator, a layout often inferred in systems exhibiting complex oscillatory dynamics.[38–40] Despite the above differences in the proposed molecular mechanisms, both modifications achieve the same end result—the appearance of oscillations and waves—by endowing the ADS model with additional negative feedback. The ADSI model does so by introducing a full negative feedback loop in which RhoA-GTP

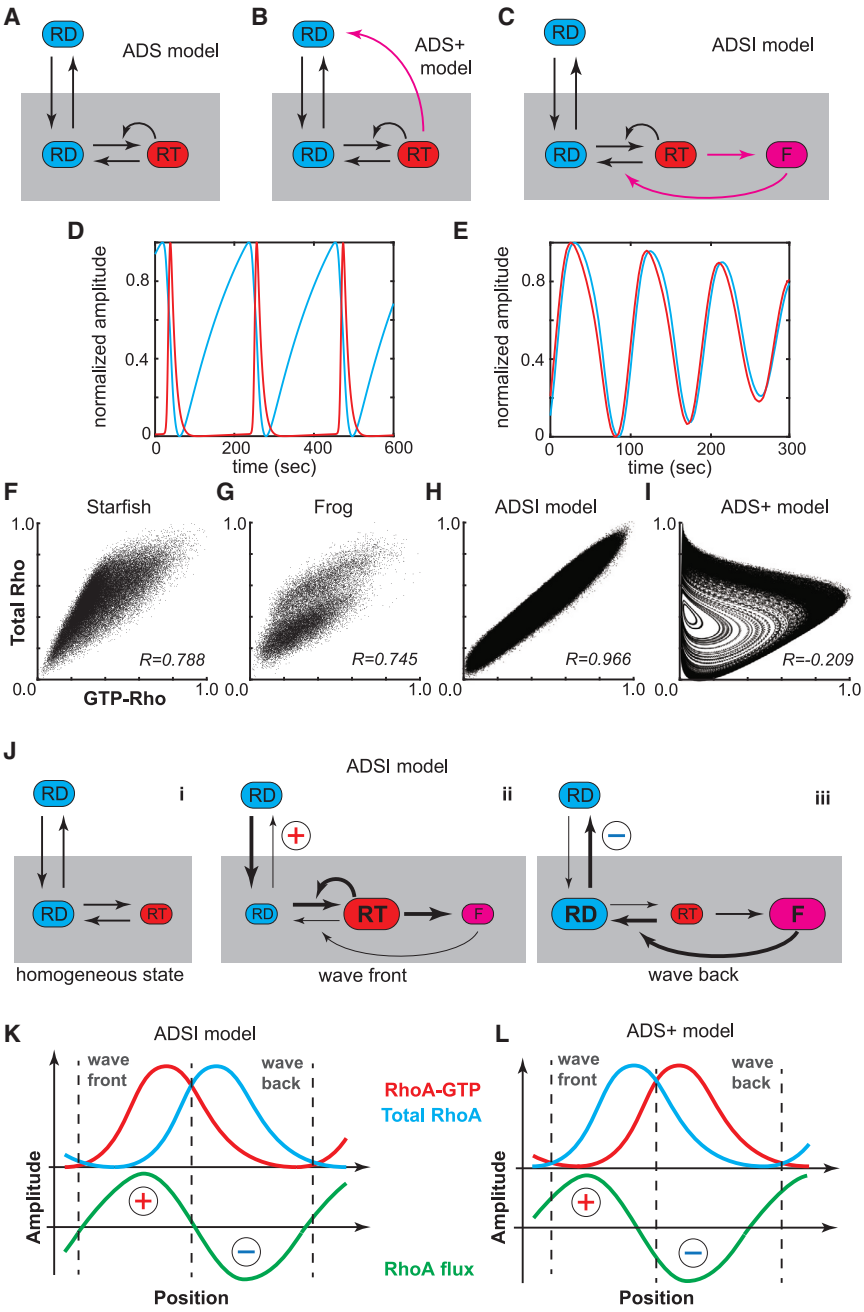

Figure 2. Comparison of the ADSI and ADS+ models of wave dynamics

(A–C) Schematic diagrams of reaction networks. RT, RhoA-GTP; RD, RhoA-GDP; F, inhibitor. Shaded area represents membrane.

(D and E) Representative time series of the spatially distributed (D) ADS+ and (E) ADSI models. Red, RT; cyan, TR (total RhoA).

(F–I) Normalized scatterplots of systems specified on figures. (F) Averaged pixel values from a starfish video; (G) same for a frog medial section video; (H) data from the spatially distributed simulation of the ADSI model; and (I) data from the spatially distributed simulation of the ADS+ model.

(J) Schematic diagrams of Rho dynamics according to the ADSI model. Sizes of labels and arrows represent relative magnitudes of molecular pools and fluxes, respectively.

(K and L) Schematic diagrams comparing spatial profiles of RT, TR, and RhoA flux predicted by (K) ADSI and (L) ADS+ models.

See also Figure S3 and Tables S1 and S2 for further discussion.

induces its own inactivation via recruiting a GAP with a delay necessary to polymerize F-actin. The ADS+ model instead compacts negative feedback into a single reaction in which GTPase inactivation and removal from the plasma membrane are combined to ensure that the inactivated GTPase cannot be immediately reactivated by a positive-feedback GEF but must first rebind the membrane from the cytoplasm.

Although the ADS+ and ADSI models have many similarities, comparison of the wave patterns predicted by the two models shows that they are qualitatively different (compare Figures 2D and 2E). The ADS+ model (Figure 2D) predicts that one period of wave dynamics involves progressive membrane accumulation of inactive RhoA followed by its rapid autocatalytic activation. RhoA-GTP thus produced is then simultaneously inactivated and removed from the membrane (magenta arrow, Figure 2B). This reaction first reverses Rho activation and then fully extinguishes the spike of RhoA activity. The ADS+ model belongs to the general class of so-called accumulate-and-fire models[41] suggested to explain pH oscillations in chemistry.[42] The accumulate-and-fire models combine phases of fast and slow changes in the concentrations of species they describe. Indeed, in Figure 2D, narrow maxima of GTPase activity with fast dynamics ("fire" phase, characteristic time $T_1 \approx 50\ s$) are interspersed by broader intervals ("accumulate" phase, characteristic time $T_2 \approx 150\ s$) of slow accumulation of total GTPase. By forcing unbinding of the GTPase from the membrane immediately after its inactivation, the ADS+ model induces local depletion of the total membrane RhoA so that the new cycle of activity starts with the replenishment of the membrane pool of inactive RhoA from the cytoplasm (Figures 2D and 2L). Consequently, the ADS+ model predicts that the dynamics of RT and TR are largely anticorrelated: within the accumulate phase, TR grows to its maximum, while RT remains essentially 0, whereas, within the fire phase, the surge in RT correlates with the drop in TR. These predictions are not consistent with the empirical results, wherein RT accumulates ahead of TR and the two signals are largely correlated. In contrast, the ADSI model (Figure 2E) predicts near-harmonic oscillations described by a single timescale ($T \approx 100\ s$), with time-shifted but otherwise largely correlated RT and TR, predictions that closely match the experimental data (Figure 1).

To quantify these qualitative observations, we offer an intuitive, heuristic approach that permits direct comparison between the models and experimental data without the need for fitting the models to a particular dataset. This approach is demonstrated in Figures 2F and 2G, where the normalized and spatially averaged intensities of imaging pixels are shown as scatterplots. Comparison of the plots shows that the clouds of data points in both starfish (Figure 2F) and frog (Figure 2G) experiments exhibit high positive correlation, in full agreement with the prediction of the ADSI model (Figure 2H). By contrast, the ADS+ model predicts a distinct distribution of data points with small negative correlation (Figure 2I).

Analysis of our experimental data in both starfish and frog also showed that the maxima of RhoA GTPase activity precede in time the maxima of the RhoA membrane abundance within all observed activity patterns, including propagating waves and pulses. Remarkably, mathematical analysis of the ADS+ and ADSI models reveals that the two models provide opposite predictions regarding the sign of the time shift between the maxima of GTPase activity and the abundance on the plasma membrane. Indeed, the ADS+ model posits that the maximum of GTPase abundance must precede the maximum of activity (Figures 2D and S3C and STAR Methods section, analysis of the ADS+ model). In contrast, and in agreement with the experiment, the ADSI model states that the maximum of activity always precedes the maximum of abundance (Figures 2E and S3F and STAR Methods section, analysis of the ADSI model). Importantly, analysis shows that these model predictions are parameter-independent and thus qualitatively differentiate the two models.

These divergent model predictions can be understood within the framework provided by the theoretical concept of GTPase flux, the notion that the membrane-cytoplasmic shuttling and, therefore, cortical patterning of Rho GTPases are coupled with their nucleotide cycling.[1,31,43–45] The ADSI model is based on the premise that RhoA-GDP undergoes rapid membrane-cytoplasmic exchange, whereas RhoA-GTP is largely membrane-bound until inactivated by GAPs. This conjecture is strongly supported by the observation that Rho GDP dissociation inhibitors (Rho GDIs), which solubilize Rho GTPases, have a higher affinity for Rho-GDP than Rho-GTP,[46–48] the demonstration that Rho GTPases in the cytoplasm are predominantly in the GDP-bound form,[49,50] and the observation that Rho-GTP is enriched on membranes.[36,51] In a spatially homogeneous steady state (i.e., in the absence of any spatial patterns), the cytoplasmic and membrane pools of inactive RhoA are in equilibrium, resulting in a zero net RhoA flux (Figure 2Ji). In a cortex exhibiting waves, activation of RhoA by positive feedback at the front of the wave drives the system out of equilibrium, leading to the local depletion of the membrane-bound pool of RhoA-GDP. This depletion is rapidly compensated for by the translocation of RhoA-GDP from the cytoplasm into the depleted region of the membrane (positive Rho flux, Figure 2Jii). The newly deposited RhoA-GDP is immediately activated on the membrane by the high local concentration of the GEF inducing further RhoA-GDP depletion and thus more compensatory RhoA-GDP deposition. Therefore, in the framework of the ADSI model, activation of GTPase drives its translocation from the cytoplasm to the membrane and causes its local enrichment. Thus, according to the ADSI model, the maximum of GTPase activity approximately coincides with the maximum of the GTPase positive flux (Figure 2K). The action of this positive-feedback loop between RhoA activation and accumulation proceeds until it is stopped by the negative feedback provided by the inhibitor. At the back of the wave, inactivation of RhoA causes the local surplus of membrane-bound RhoA-GDP that is recycled back to the cytoplasm (negative Rho flux, Figures 2Jiii and 2K).

The difference in the behavior of the ADS+ model is explained by the addition of the reaction of simultaneous inactivation and recycling to the cytoplasm (magenta arrow, Figures 2B and S3A). For the oscillations and waves to exist within the ADS+ model, the rate of this reaction must be much greater than the off rate of the inactive GTPase (see STAR Methods). Thus, in the framework of the ADS+ model, and contrary to the main assumption of the ADSI model, the membrane residence time of RhoA-GTP is much shorter than that of RhoA-GDP and the roles of active and inactive forms are effectively reversed. To put it another way, in the ADSI model, activation stabilizes the GTPase on the membrane, whereas in the ADS+ model, activation effectively removes the GTPase from the membrane. Thus, the ADS+ model posits that the maximum of RhoA activity coincides with the maximum of the negative flux of RhoA (Figure 2L). This is the fundamental difference in the main assumptions of the two models and it explains the different sign of the time shift predicted between the maxima of RT and TR. Furthermore, it also explains the existence of strong positive correlation between RT and TR in the ADSI model and weak negative correlation in the ADS+ model (Figures 2H and 2I).

Therefore, the sign of the time shift between the maxima of total RhoA and active RhoA qualitatively separates the two theoretical models of wave generation. We conclude that our data shown in Figure 1 argue strongly in favor of the ADSI model and falsify the ADS+ model. As shown in Figure S3G, this conclusion is robust to the unknown time delay between the true maximum of the GTPase activity and that of the fluorescent signal of the probe for active RhoA used in our experiments. Indeed, due to this delay, the true maximum of RhoA activity (dashed red curve in Figure S3G, top) is even further ahead of the maximum of total RhoA (solid blue curve) than the experimentally measured maximum of the reporter accumulation (solid red curve). However, if the ADS+ model held true, the experimentally measured maximum of the activity probe would be even further behind the maximum of total RhoA than the true maximum of RhoA activity (Figure S3G, bottom).

Although the results presented here show that a simple ADS model based solely on RhoA-GTP autoactivation and RhoA-GDP depletion cannot account for RhoA activity waves, they leave open the intriguing possibility that some other player necessary for RhoA activation might be subject to depletion and thus influence the wave dynamics. For example, Tong et al. recently suggested that depletion of PI(4,5)P2 could regulate the period of mitotic Rho waves in mast cells,[38] a possibility consistent with the results presented here, assuming that the lipid operates on, say, the GEF rather than the Rho-GDP.

In summary, we found that waves of GTPase activity are unambiguously associated with the waves of GTPase enrichment, consistent with recent results from cell repair[17] and yeast polarization.[19] Furthermore, in both frogs and starfish, RhoA activity waves precede waves of RhoA enrichment, a finding that excludes the ADS+ model, which predicts the opposite result. These observations indirectly support the existence of explicit

inhibitory molecular complexes that are induced by the activity of GTPases and eventually extinguish it. Negative feedback mediated by a GAP bound to a polymeric network generated downstream of the activity of a small GTPase is likely broadly conserved.[1,4] For example, binding of the Cdc42 GAP Bem2 to the septin scaffold was shown to provide negative feedback to Cdc42 activity in the context of budding yeast polarization.[52] The results presented here also bring into sharper focus the notion of Rho flux between the cytoplasm and the plasma membrane as a result of the combined action of positive and negative feedback loops, an idea previously only tested for Cdc42 in budding and fission yeast.[53–55] Given the recent demonstrations of close collaboration between Rho GEFs and GAPs in a variety of model systems and cellular contexts,[11,12,56] these findings indicate that the Rho flux is likely to be a core feature of Rho GTPases in cell-morphogenetic activity.

RESOURCE AVAILABILITY

Lead contact

Requests for further information and resources should be directed to and will be fulfilled by the lead contact, William M. Bement (wmbement@wisc.edu).

Materials availability

- Frog ovary was obtained either by surgically extracting it from adult female wild-type *Xenopus laevis* purchased from the Marine Biological Laboratory and Xenopus 1 or by ordering ovary directly from Xenopus 1.
- Starfish oocytes were obtained from Marinus and South Coast Bio-Marine.
- Plasmids generated for this study (listed in the key resources table) are available upon request from the lead contact with the completed material transfer agreements (MTAs).

Data and code availability

- All data reported in this paper will be shared by the lead contact upon request.
- All code used to analyze the data in this study can be found in the key resources table. This paper does not report original code.
- Any additional information required to reanalyze the data reported in this work paper is available from the lead contact upon request.

ACKNOWLEDGMENTS

A.B.G. acknowledges financial support from the Leverhulme Trust (RPG-2020-220) and from the Biotechnology and Biological Sciences Research Council (BB/W013614/1). W.M.B. acknowledges financial support from the National Institutes of Health (RO1GM052932) and the National Science Foundation (2132606).

AUTHOR CONTRIBUTIONS

D.C. and A.E.G. designed and prepared key reagents; D.C., G.v.D., and W.B. designed and conducted wet-lab experiments; M.L. and A.B.G. designed and conducted modeling experiments; D.C., W.B., A.B.G., M.L., G.v.D., and A.E.G. wrote and edited the paper; W.B., G.v.D., and A.B.G. were responsible for oversight, administration, and funding of the work.

DECLARATION OF INTERESTS

The authors declare no competing financial interests.

STAR★METHODS

Detailed methods are provided in the online version of this paper and include the following:

SUPPLEMENTAL INFORMATION

Supplemental information can be found online at https://doi.org/10.1016/j.cub.2025.02.003.

Received: April 10, 2024
Revised: January 6, 2025
Accepted: February 3, 2025
Published: February 25, 2025

REFERENCES

1. Bement, W.M., Goryachev, A.B., Miller, A.L., and von Dassow, G. (2024). Patterning of cell cortex by Rho GTPases. Nat. Rev. Mol. Cell Biol. *25*, 290–308. https://doi.org/10.1038/s41580-023-00682-z.
2. Michaud, A., Swider, Z.T., Landino, J., Leda, M., Miller, A.L., von Dassow, G., Goryachev, A.B., and Bement, W.M. (2021). Cortical excitability and cell division. Curr. Biol. *31*, R553–R559. https://doi.org/10.1016/j.cub.2021.02.053.
3. Bement, W.M., Leda, M., Moe, A.M., Kita, A.M., Larson, M.E., Golding, A.E., Pfeuti, C., Su, K.C., Miller, A.L., Goryachev, A.B., and von Dassow, G. (2015). Activator-inhibitor coupling between Rho signalling and actin assembly makes the cell cortex an excitable medium. Nat. Cell Biol. *17*, 1471–1483. https://doi.org/10.1038/ncb3251.
4. Michaud, A., Leda, M., Swider, Z.T., Kim, S., He, J., Landino, J., Valley, J.R., Huisken, J., Goryachev, A.B., von Dassow, G., and Bement, W.M. (2022). A versatile cortical pattern-forming circuit based on Rho, F-actin, Ect2, and RGA-3/4. J. Cell Biol. *221*, e202203017. https://doi.org/10.1083/jcb.202203017.
5. Beta, C., Edelstein-Keshet, L., Gov, N., and Yochelis, A. (2023). From actin waves to mechanism and back: How theory aids biological understanding. eLife *12*, e87181. https://doi.org/10.7554/eLife.87181.
6. Swider, Z.T., Michaud, A., Leda, M., Landino, J., Goryachev, A.B., and Bement, W.M. (2022). Cell cycle and developmental control of cortical excitability in Xenopus laevis. Mol. Biol. Cell *33*, ar73. https://doi.org/10.1091/mbc.E22-01-0025.
7. Graessl, M., Koch, J., Calderon, A., Kamps, D., Banerjee, S., Mazel, T., Schulze, N., Jungkurth, J.K., Patwardhan, R., Solouk, D., et al. (2017). An excitable Rho GTPase signaling network generates dynamic subcellular contraction patterns. J. Cell Biol. *216*, 4271–4285. https://doi.org/10.1083/jcb.201706052.
8. Burkel, B.M., Benink, H.A., Vaughan, E.M., von Dassow, G., and Bement, W.M. (2012). A Rho GTPase signal treadmill backs a contractile array. Dev. Cell *23*, 384–396. https://doi.org/10.1016/j.devcel.2012.05.025.
9. Werner, M.E., Ray, D.D., Breen, C., Staddon, M.F., Jug, F., Banerjee, S., and Maddox, A.S. (2024). Mechanical and biochemical feedback combine to generate complex contractile oscillations in cytokinesis. Curr. Biol. *34*, 3201–3214.e5. https://doi.org/10.1016/j.cub.2024.06.037.
10. Xiao, S., Tong, C., Yang, Y., and Wu, M. (2017). Mitotic Cortical Waves Predict Future Division Sites by Encoding Positional and Size Information. Dev. Cell *43*, 493–506.e3. https://doi.org/10.1016/j.devcel.2017.10.023.

11. Michaux, J.B., Robin, F.B., McFadden, W.M., and Munro, E.M. (2018). Excitable RhoA dynamics drive pulsed contractions in the early C. elegans embryo. J. Cell Biol. *217*, 4230–4252. https://doi.org/10.1083/jcb.201806161.

12. Jackson, J.A., Denk-Lobnig, M., Kitzinger, K.A., and Martin, A.C. (2024). Change in RhoGAP and RhoGEF availability drives transitions in cortical patterning and excitability in Drosophila. Curr. Biol. *34*, 2132–2146.e5. https://doi.org/10.1016/j.cub.2024.04.021.

13. Goryachev, A.B., Leda, M., Miller, A.L., von Dassow, G., and Bement, W.M. (2016). How to make a static cytokinetic furrow out of traveling excitable waves. Small GTPases *7*, 65–70. https://doi.org/10.1080/21541248.2016.1168505.

14. Tan, T.H., Liu, J., Miller, P.W., Tekant, M., Dunkel, J., and Fakhri, N. (2020). Topological turbulence in the membrane of a living cell. Nat. Phys. *16*, 657–662. https://doi.org/10.1038/s41567-020-0841-9.

15. Wigbers, M.C., Tan, T.H., Brauns, F., Liu, J., Swartz, S.Z., Frey, E., and Fakhri, N. (2021). A hierarchy of protein patterns robustly decodes cell shape information. Nat. Phys. *17*, 578–584. https://doi.org/10.1038/s41567-021-01164-9.

16. Landino, J., Leda, M., Michaud, A., Swider, Z.T., Prom, M., Field, C.M., Bement, W.M., Vecchiarelli, A.G., Goryachev, A.B., and Miller, A.L. (2021). Rho and F-actin self-organize within an artificial cell cortex. Curr. Biol. *31*, 5613–5621.e5. https://doi.org/10.1016/j.cub.2021.10.021.

17. Golding, A.E., Visco, I., Bieling, P., and Bement, W.M. (2019). Extraction of active RhoGTPases by RhoGDI regulates spatiotemporal patterning of RhoGTPases. eLife *8*, e50471. https://doi.org/10.7554/eLife.50471.

18. Bi, E., Chiavetta, J.B., Chen, H., Chen, G.C., Chan, C.S., and Pringle, J.R. (2000). Identification of novel, evolutionarily conserved Cdc42p-interacting proteins and of redundant pathways linking Cdc24p and Cdc42p to actin polarization in yeast. Mol. Biol. Cell *11*, 773–793. https://doi.org/10.1091/mbc.11.2.773.

19. Bendezú, F.O., Vincenzetti, V., Vavylonis, D., Wyss, R., Vogel, H., and Martin, S.G. (2015). Spontaneous Cdc42 polarization independent of GDI-mediated extraction and actin-based trafficking. PLoS Biol. *13*, e1002097. https://doi.org/10.1371/journal.pbio.1002097.

20. Lu, M.S., and Drubin, D.G. (2020). Cdc42 GTPase regulates ESCRTs in nuclear envelope sealing and ER remodeling. J. Cell Biol. *219*, e201910119. https://doi.org/10.1083/jcb.201910119.

21. Yonemura, S., Hirao-Minakuchi, K., and Nishimura, Y. (2004). Rho localization in cells and tissues. Exp. Cell Res. *295*, 300–314. https://doi.org/10.1016/j.yexcr.2004.01.005.

22. Benink, H.A., and Bement, W.M. (2005). Concentric zones of active RhoA and Cdc42 around single cell wounds. J. Cell Biol. *168*, 429–439. https://doi.org/10.1083/jcb.200411109.

23. Bischof, J., Brand, C.A., Somogyi, K., Májer, I., Thome, S., Mori, M., Schwarz, U.S., and Lénárt, P. (2017). A cdk1 gradient guides surface contraction waves in oocytes. Nat. Commun. *8*, 849. https://doi.org/10.1038/s41467-017-00979-6.

24. Liu, J., Totz, J.F., Miller, P.W., Hastewell, A.D., Chao, Y.C., Dunkel, J., and Fakhri, N. (2021). Topological braiding and virtual particles on the cell membrane. Proc. Natl. Acad. Sci. USA *118*, e2104191118. https://doi.org/10.1073/pnas.2104191118.

25. Gierer, A., and Meinhardt, H. (1972). A theory of biological pattern formation. Kybernetik *12*, 30–39. https://doi.org/10.1007/BF00289234.

26. Murray, J.D. (1993). Mathematical Biology (Springer-Verlag). https://doi.org/10.1007/978-3-662-08542-4.

27. Goryachev, A.B., and Leda, M. (2019). Autoactivation of small GTPases by the GEF-effector positive feedback modules. F1000Res *8*, F1000FacultyRev-1676. https://doi.org/10.12688/f1000research.20003.1.

28. Jackson, C.L. (2014). GEF-effector interactions. Cell. Logist. *4*, e943616. https://doi.org/10.4161/21592780.2014.943616.

29. Rousso, T., Schejter, E.D., and Shilo, B.Z. (2016). Orchestrated content release from Drosophila glue-protein vesicles by a contractile actomyosin network. Nat. Cell Biol. *18*, 181–190. https://doi.org/10.1038/ncb3288.

30. Segal, D., Zaritsky, A., Schejter, E.D., and Shilo, B.Z. (2018). Feedback inhibition of actin on Rho mediates content release from large secretory vesicles. J. Cell Biol. *217*, 1815–1826. https://doi.org/10.1083/jcb.201711006.

31. Goryachev, A.B., and Pokhilko, A.V. (2008). Dynamics of Cdc42 network embodies a Turing-type mechanism of yeast cell polarity. FEBS Lett. *582*, 1437–1443. https://doi.org/10.1016/j.febslet.2008.03.029.

32. Mori, Y., Jilkine, A., and Edelstein-Keshet, L. (2008). Wave-pinning and cell polarity from a bistable reaction-diffusion system. Biophys. J. *94*, 3684–3697. https://doi.org/10.1529/biophysj.107.120824.

33. Howell, A.S., Savage, N.S., Johnson, S.A., Bose, I., Wagner, A.W., Zyla, T.R., Nijhout, H.F., Reed, M.C., Goryachev, A.B., and Lew, D.J. (2009). Singularity in polarization: rewiring yeast cells to make two buds. Cell *139*, 731–743. https://doi.org/10.1016/j.cell.2009.10.024.

34. Goryachev, A.B., and Leda, M. (2017). Many roads to symmetry breaking: molecular mechanisms and theoretical models of yeast cell polarity. Mol. Biol. Cell *28*, 370–380. https://doi.org/10.1091/mbc.E16-10-0739.

35. Frey, E., and Brauns, F. (2022). Self-organization of Protein Patterns. In Active Matter and Nonequilibrium Statistical Physics: Lecture Notes of the Les Houches Summer School, J. Tailleur, G. Gompper, M.C. Marchetti, J.M. Yeomans, and C. Salomon, eds. (Oxford University Press), pp. 347–445. https://doi.org/10.1093/oso/9780192858313.003.0011.

36. Hodge, R.G., and Ridley, A.J. (2016). Regulating Rho GTPases and their regulators. Nat. Rev. Mol. Cell Biol. *17*, 496–510. https://doi.org/10.1038/nrm.2016.67.

37. Bos, J.L., Rehmann, H., and Wittinghofer, A. (2007). GEFs and GAPs: critical elements in the control of small G proteins. Cell *129*, 865–877. https://doi.org/10.1016/j.cell.2007.05.018.

38. Tong, C.S., Xu, X.J., and Wu, M. (2023). Periodicity, mixed-mode oscillations, and multiple timescale in a phosphoinositide-Rho GTPase network. Cell Rep. *42*, 112857. https://doi.org/10.1101/2023.05.22.541800.

39. Yochelis, A., Flemming, S., and Beta, C. (2022). Versatile patterns in the actin cortex of motile cells: self-organized pulses can coexist with macropinocytic ring-shaped waves. Phys. Rev. Lett. *129*, 088101. https://doi.org/10.1103/PhysRevLett.129.088101.

40. Yochelis, A. (2021). The nonlinear initiation of side-branching by activator-inhibitor-substrate (Turing) morphogenesis. Chaos *31*, 051102. https://doi.org/10.1063/5.0050630.

41. Pikovsky, A., Rosenblum, M., and Kurths, J. (2001). Synchronization (University Press). https://doi.org/10.1017/CBO9780511755743.

42. Epstein, I.R., and Pojman, J.A. (1998). An Introduction in Nonlinear Chemical Dynamics (Oxford University Press).

43. Bement, W.M., Miller, A.L., and von Dassow, G. (2006). Rho GTPase activity zones and transient contractile arrays. BioEssays *28*, 983–993. https://doi.org/10.1002/bies.20477.

44. Goryachev, A.B., and Pokhilko, A.V. (2006). Computational model explains high activity and rapid cycling of Rho GTPases within protein complexes. PLoS Comput. Biol. *2*, e172. https://doi.org/10.1371/journal.pcbi.0020172.

45. Miller, A.L., and Bement, W.M. (2009). Regulation of cytokinesis by Rho GTPase flux. Nat. Cell Biol. *11*, 71–77. https://doi.org/10.1038/ncb1814.

46. Cherfils, J., and Zeghouf, M. (2013). Regulation of small GTPases by GEFs, GAPs, and GDIs. Physiol. Rev. *93*, 269–309. https://doi.org/10.1152/physrev.00003.2012.

47. Johnson, J.L., Erickson, J.W., and Cerione, R.A. (2009). New insights into how the Rho guanine nucleotide dissociation inhibitor regulates the interaction of Cdc42 with membranes. J. Biol. Chem. *284*, 23860–23871. https://doi.org/10.1074/jbc.M109.031815.

48. Tnimov, Z., Guo, Z., Gambin, Y., Nguyen, U.T., Wu, Y.W., Abankwa, D., Stigter, A., Collins, B.M., Waldmann, H., Goody, R.S., and Alexandrov, K. (2012). Quantitative analysis of prenylated RhoA interaction with its chaperone, RhoGDI. J. Biol. Chem. *287*, 26549–26562. https://doi.org/10.1074/jbc.M112.371294.

49. Hall, A., Paterson, H.F., Adamson, P., and Ridley, A.J. (1993). Cellular responses regulated by rho-related small GTP-binding proteins. Philos. Trans. R. Soc. Lond. B Biol. Sci. *340*, 267–271. https://doi.org/10.1098/rstb.1993.0067.

50. Heasman, S.J., and Ridley, A.J. (2008). Mammalian Rho GTPases: new insights into their functions from in vivo studies. Nat. Rev. Mol. Cell Biol. *9*, 690–701. https://doi.org/10.1038/nrm2476.

51. Park, H.O., and Bi, E. (2007). Central roles of small GTPases in the development of cell polarity in yeast and beyond. Microbiol. Mol. Biol. Rev. *71*, 48–96. https://doi.org/10.1128/MMBR.00028-06.

52. Okada, S., Leda, M., Hanna, J., Savage, N.S., Bi, E., and Goryachev, A.B. (2013). Daughter cell identity emerges from the interplay of Cdc42, septins, and exocytosis. Dev. Cell *26*, 148–161. https://doi.org/10.1016/j.devcel.2013.06.015.

53. Witte, K., Strickland, D., and Glotzer, M. (2017). Cell cycle entry triggers a switch between two modes of Cdc42 activation during yeast polarization. eLife *6*, e26722. https://doi.org/10.7554/eLife.26722.

54. Goryachev, A.B., and Leda, M. (2017). Cell Polarity: Spot-On Cdc42 Polarization Achieved on Demand. Curr. Biol. *27*, R810–R812. https://doi.org/10.1016/j.cub.2017.07.006.

55. Lamas, I., Merlini, L., Vještica, A., Vincenzetti, V., and Martin, S.G. (2020). Optogenetics reveals Cdc42 local activation by scaffold-mediated positive feedback and Ras GTPase. PLoS Biol. *18*, e3000600. https://doi.org/10.1371/journal.pbio.3000600.

56. Imran Alsous, J., Romeo, N., Jackson, J.A., Mason, F.M., Dunkel, J., and Martin, A.C. (2021). Dynamics of hydraulic and contractile wave-mediated fluid transport during Drosophila oogenesis. Proc. Natl. Acad. Sci. USA *118*, e2019749118. https://doi.org/10.1073/pnas.2019749118.

57. Schindelin, J., Arganda-Carreras, I., Frise, E., Kaynig, V., Longair, M., Pietzsch, T., Preibisch, S., Rueden, C., Saalfeld, S., Schmid, B., et al. (2012). Fiji: an open-source platform for biological-image analysis. Nat. Methods *9*, 676–682. https://doi.org/10.1038/nmeth.2019.

58. Vanag, V.K., and Epstein, I.R. (2009). Pattern formation mechanisms in reaction-diffusion systems. Int. J. Dev. Biol. *53*, 673–681. https://doi.org/10.1387/ijdb.072484vv.

STAR★METHODS

KEY RESOURCES TABLE

REAGENT or RESOURCE	SOURCE	IDENTIFIER
Critical commercial assays		
mMessage Machine SP6 kit	Ambion	AM1340
Poly(A) Tailing kit	Ambion	AM1350
RNA clean-up kit (RNeasy Kit)	Qiagen	74104
Experimental models: Organisms/strains		
Xenopus laevis sexually mature females	Xenopus 1 and Marine Biological Lab	N/A
Patiria Miniata	Marinus and South Coast Bio-Marine	N/A
Recombinant DNA		
pCS2_mCh-rGBD	Benink and Bement[22]	N/A
pCS2_GFP-rGBD	Benink and Bement[22]	N/A
pCS2_GFP-IT-xRho (frog experiments)	Golding et al.[17]	N/A
pCS2_xGDI (frog experiments)	Golding et al.[17]	N/A
pCS2_xEct2^{dNLS} (frog experiments)	Michaud et al.[4]	N/A
pCS2_xRGA-3/4 (frog experiments)	Michaud et al.[4]	N/A
pCS2_GFP-IT-PmRho (starfish experiments)	This study	N/A
pCS2_SpEct2 (starfish experiments)	Bement et al.[3]	N/A
Software and algorithms		
Wave analysis Python script	Swider et al.[6]; updated for kymograph analysis in this study	https://github.com/zacswider/waveAnalysis
MATLAB scripts for image analysis	This study	https://doi.org/10.5281/zenodo.14582898
MATLAB	MathWorks	https://www.mathworks.com/products/matlab.html
Fiji/ImageJ	Schindelin et al.[57]	https://imagej.nih.gov/ij/
Fiji/ImageJ Plugins	This study	https://github.com/domchom/DC_Fiji_macros
Prism	GraphPad	https://www.graphpad.com

EXPERIMENTAL MODEL AND STUDY PARTICIPANT DETAILS

Adult *Patiria miniata* (bat stars) were obtained from Marinus and South Coast Bio-Marine and housed in natural seawater tanks with aeration at 11°-14°C, at the Oregon Institute of Marine Biology. Animals were fed with minced, cooked shrimp and locally collected mussels. Starfish oocytes were obtained from ovary fragments, after transfer to Ca^{2+}-free artificial seawater. Individual oocytes were kept at 12°C and rinsed several times to remove follicles and then transferred to filtered sea water at 12°C until microinjection.

Adult wild-type *Xenopus laevis* (frog) females were purchased from the Marine Biological Laboratory and Xenopus 1 and housed in tanks connected to a continuous-flow Tecniplast system. The water was maintained at a temperature of 18–19°C, a pH of 7.2–7.8, and a conductivity of 1300–1400 μS. Frogs were fed Nasco Frog Brittle twice per week. Chunks of ovary were collected from adult wild-type *Xenopus laevis* females and stored in 1x Barth's solution (87.4 mM NaCl, 1 mM KCl, 2.4 mM $NaHCO_3$, 0.82 mM $MgSO_4$, 0.6 mM $NaNO_3$, 0.7 mM $CaCl_2$, and 10 mM HEPES at pH 7.6). Oocytes were treated with collagenase for 1 hr at 16°C, and then rinsed extensively with 1x Barth's solution before recovering overnight at 16°C. Stage VI oocytes were selected and manually defolliculated before injection.

METHOD DETAILS

Constructs and mRNA

All constructs are contained within the pCS2+ vector. The GFP- and mCherry-rGBD used in both starfish and frog experiments were generated by fusing the Rho binding domain of Rhoketin with a fluorescent protein.[22] For frog IT-GFP-RhoA and IT-mCh-RhoA, the constructs were created by inserting a GFP/mCherry protein into an exposed loop of the RhoA protein.[17] A starfish version of IT-GFP-RhoA was developed using a similar approach, where a GFP was introduced within an external loop of the *P. miniata* RhoA. The GDI utilized in this study was previously detailed in Golding et al.[17] The Ect2^{dNLS} and RGA-3/4 constructs employed for inducing cortical

excitability in frogs were described elsewhere.[4] For starfish experiments, we utilized the previously described echinoderm Ect2 construct.[3]

Prior to mRNA synthesis, all plasmids were linearized downstream of the open reading frame. mRNA synthesis was then carried out using the mMessage Machine SP6 kit (Ambion, #AM1340). For starfish mRNA, polyadenylation was performed using the Poly(A) Tailing kit (Ambion, #AM1350). mRNA was subsequently purified using the RNeasy Kit (Qiagen, #74104). Size and quality of mRNA was confirmed via gel electrophoresis, and concentration was calculated against a GFP standard curve.

Microinjection

Starfish oocytes were sheared with a narrow capillary to remove mucus and arranged in rows on coverslip-bottomed dishes (MatTek) that were pre-rinsed with 1% protamine sulphate for 30 sec. Oocytes were then pressure-injected using capillary glass needles using a Dagan Instruments injector and an Narishige oil-hydraulic micromanipulator. An injection volume corresponding to 1–2% of the total oocyte volume was used and, after injection with mRNA, oocytes were incubated overnight at 12–14°C. The injection needle concentration of IT-GFP-RhoA, Ect2, and rGBD mRNA were 25-50 ng/μL, 50-80 ng/μL, and 50-100 ng/μL, respectively.

Frog oocyte microinjections were performed using a Warner Instruments PLI-100 microinjector and a manual Narishige micromanipulator. Needles were pulled from capillary tubes and calibrated to inject 40 nL of mRNA. Cells were injected in a mesh-bottomed Petri dish containing 1× Barth's solution. For IT-GFP-RhoA, GDI, and rGBD, mRNA was injected the day before imaging and incubated overnight at 16°C. The injection needle concentration of IT-RhoA, GDI, and rGBD mRNA were 250 ng/μL, 125 ng/μL, and 100 ng/μL, respectively. For $Ect2^{dNLS}$ and RGA-3/4, the mRNA was injected the morning of imaging, and the cells were incubated at 23°C for >3-4 hours before imaging to allow for cortical wave generation. The injection needle concentration of $Ect2^{dNLS}$ and RGA-3/4 mRNA were 200 ng/μL and 166 ng/μL, respectively, unless stated otherwise.

Image acquisition

Starfish oocytes were screened for mRNA expression (as judged with a fluorescent dissecting scope) and small groups were selected for imaging. Oocyte maturation was induced by addition of 1-methyladenine to $\sim 10^{-5}$ M. Oocytes were imaged in chambers made by placing 22x30 mm #1.5 coverslips on ~1 cm lines of vacuum grease drawn on 75x25 mm glass slides with toothpicks. Imaging was conducted on an inverted Olympus FluoView 1000 laser-scanning confocal microscope using a 1.15-NA 40× water-immersion objective. Temperature was maintained at 16–18°C by room air conditioning; these temperatures are well within the range tolerated by *P. miniata*.

Frog oocytes were mounted onto glass slides within a ~1x1 cm area of vacuum grease to accommodate their size and were covered with #1.5 coverslips in 1x Barth's solution. Imaging was conducted using a Prairie View Swept Field Confocal (SFC) system mounted on a Nikon Eclipse Ti base (Bruker), employing a 60x 1.4-NA oil immersion objective. The microscope was controlled by Prairie View software (Bruker). Imaging was conducted at room temperature. *En face* imaging was performed by acquiring time-series data with 5 steps of 1 μm each. For medial section imaging, images were captured in a single optical plane.

Image processing

Image processing was performed using ImageJ/Fiji.[57] Multi-stack *en face* images were max projected, then subsequently divided by the sum of pixel intensities to mitigate vertical artifacts stemming from the SFC microscope. Difference videos were generated in Fiji through the process of subtracting the signal from n frames following a frame of interest from each corresponding frame. Kymographs were generated using Fiji's reslice function, with a 1-pixel-wide line across the field of view for en-face imaging or along the cell edge for medial section imaging. All images and figures were compiled in Adobe Illustrator.

QUANTIFICATION AND STATISTICAL ANALYSES

Image analysis

The analyses depicted in Figure 1, including time-shift, period, and wave profile analyses, were conducted using the "WaveAnalysis" Python script.[6] For medial sectional imaging, kymographs were generated and assessed using the same script, with modifications tailored to accommodate kymographs (these adaptations are now integrated into the script and detailed here: https://github.com/zacswider/waveAnalysis). In short, kymographs were vertically binned into lines approximately 4 microns wide, and the average pixel intensity across those 4 μm was used to construct wave profiles. Subsequent analyses were the same as the previously reported procedures.[6] For wave profiles in Figure 1, the signal intensity was normalized to the maximum and minimum signal via

$$Normalized\ value = \frac{Raw\ value - Min\ value}{Max\ value - Min\ value}.$$

The mean time-shifts illustrated in Figure S1E were produced utilizing a previously described MATLAB script.[16] Difference videos were utilized for all quantitative assessments. Figures were initially crafted in GraphPad Prism and subsequently refined and compiled in Adobe Illustrator. Statistical analyses were conducted using GraphPad Prism.

Scatter plots (Figures 2F and 2G) were generated as follows. Fluorescent intensity signals of RhoA-GTP and total Rho were averaged within the boxes of 10x10 pixels. The resulting values were then normalized by the maximum and minimum values computed over all pixel boxes and all imaging frames of the respective imaging series using the same formula above. Correlation coefficients (Figures 2F and 2G) were computed using the MathWorks MATLAB® function *corrcoef*.

Numeric simulations

Simulations of the ADSI model[4] (Figures 2E and 2H) were performed on a square domain $200\mu m$ x $200\mu m$ with spatial resolution $\Delta x = 0.5\ \mu m$ and periodic boundary conditions for the earlier published set of parameters[4] (Table S2). The simulations were initiated with random initial conditions spatially distributed in the vicinity of the uniform stationary state.

Simulations of the ADS+ model (Figures 2D,I) were performed on a square domain $100\mu m$ x $100\mu m$ with spatial resolution $\Delta x = 0.2\ \mu m$ and periodic boundary conditions for the parameter values presented in Table S1 and $k_2 = 0.06\ \mu M^{-2}\ sec^{-1}$. To induce wave dynamics, four spiral cores were embedded into the initial conditions.

Simulation results shown as scatter plots (Figures 2H and 2I) were averaged inside the boxes of size 5x5 computational pixels and then normalized as described above (see image analysis). Correlation coefficients (Figures 2H and 2I) were computed using the MathWorks MATLAB® function *corrcoef*.

Analysis of the ADS+ model

We can quantitatively formulate the ADS+ model that describes the spatio-temporal dynamics of the two membrane-associated forms of RhoA, inactive RhoA with the local concentration RD and active RhoA with the local concentration RT as a system of two partial differential equations. Following earlier published work[15,35] but assuming for simplicity that the cytoplasmic pool of inactive RhoA is so large that its concentration can be considered constant, we write:

$$\begin{aligned} \dot{RT} &= \left(k_1 + k_2 RT^2\right) RD - (k_3 + k_4) RT + d_{RT} \Delta RT \\ \dot{RD} &= -\left(k_1 + k_2 RT^2\right) RD + k_3 RT + k_5 - k_6 RD + d_{RD} \Delta RD \end{aligned}, \qquad \text{(Equation 1)}$$

where the numbering of constants follows Figure S3A and their representative values are given in Table S1. Phase diagram of the model (1) schematically shown in Figure S3B on the plane of parameters k_4 and k_2 that quantify the strengths of negative and positive feedback, respectively, shows that the ADS+ model can support waves ubiquitously. Outside of the oscillatory domain the homogeneous steady state of the model is linearly stable, but to the right of the domain of oscillations it can be induced to produce excitable waves by a supercritical perturbation. In the following discussion we omit the diffusion terms $d_{RT}\Delta RT$, $d_{RD}\Delta RD$ and instead of RD, which cannot be assayed experimentally, we introduce the concentration of total RhoA $TR = RT + RD$, whose dynamics can be directly compared with that of IT-RhoA in experiments. This changes model (1) to the system of two ordinary differential equations:

$$\begin{aligned} \dot{RT} &= \left(k_1 + k_2 RT^2\right)(TR - RT) - (k_3 + k_4) RT \\ \dot{TR} &= k_5 - k_6 (TR - RT) - k_4 RT \end{aligned} \qquad \text{(Equation 2)}$$

As a two-variable system of ordinary differential equations, model (2) can be fully characterized mathematically in terms of the analysis of its nullclines.[26] The nullclines of equations (2), obtained by solving $\dot{RT} = 0, \dot{TR} = 0$, are then

$$TR = \frac{\left(k_1 + k_3 + k_4 + k_2 RT^2\right) RT}{k_1 + k_2 RT^2}, \dot{RT} = 0, \qquad \text{(Equation 3)}$$

and

$$TR = \frac{k_5}{k_6} + \left(1 - \frac{k_4}{k_6}\right) RT, \dot{TR} = 0 \qquad \text{(Equation 4)}$$

Existence of waves in the full spatially distributed model (1) requires that the nullclines (3,4) of the ordinary differential equations (2) satisfy the following conditions. First, nullcline (4) $\dot{TR} = 0$, which is a straight line, must have a negative slope. Second, nonlinear nullcline (3) $\dot{RT} = 0$ should have a descending segment with negative slope. An example of a phase portrait in which both conditions are satisfied is shown in Figure S3C. In this case, the point of intersection of the two nullclines corresponds to an unstable steady state of the type focus[26] (empty circle, Figure S3C), which is surrounded by a stable limit cycle (green trajectory, Figure S3C).

These conditions impose strong restrictions on the model parameters. Indeed, for the nullcline $\dot{TR} = 0$ to have a negative slope, the rate of RT membrane detachment, k_4, must be larger than that of the inactive RD, k_6, (in practice, however, the requirement is even stronger, $k_4 \gg k_6$). If the reaction of simultaneous inactivation and removal of the GTPase into the cytoplasm does not exist ($k_4 = 0$ and the magenta arrow is removed from the diagrams in Figures 2B and S3A) the ADS+ model reverts back to the basic ADS model shown in Figure 2A. The systems (1) and (2) then describe the dynamics of the ADS model and nullcline (4), $\dot{TR} = 0$, has a parameter-independent positive slope 1. Then, under varying model parameters, the nullclines either do not intersect or intersect in two points. In both cases, due to the lack of mass conservation in (2), there exists also a stable steady state corresponding to the infinite values of RT and TR. The ADS model, therefore, could be either mono- or bistable, but cannot exhibit oscillatory or excitable dynamics. This explains why the basic ADS model shown in Figure 2A cannot explain GTPase waves and requires introduction of additional elements, such as the reaction with rate k_4 (Figures 2B and S3A), or an additional inhibitory variable (Figures 2C and S3D).

An important biological conclusion that immediately follows from the requirement

$$k_4 \gg k_6 \qquad \text{(Equation 5)}$$

is that the ADS+ model (1) can explain cortical waves of GTPase activity only if the membrane residence time of active form of the GTPase is much shorter than that of its inactive form.

On the other hand, nullcline (3), $\dot{RT} = 0$, is a nonlinear function that has a sigmoidal shape with a descending segment only when $k_1 < (k_3 + k_4)/8$, which can be readily seen from the analysis of the shape of nullcline (3). This strict inequality can be approximated by

$$k_3 + k_4 \gg k_1, \qquad \text{(Equation 6)}$$

which could be biologically interpreted as a requirement that the rate of non-autocatalytic activation of a GTPase, k_1, should be small in comparison with the total rate of GTPase inactivation, $k_3 + k_4$. In comparison with (5), this requirement is, however, much less restrictive.

Another important biological conclusion arises from the analysis of the direction of phase flow determined by the equations (2). This analysis shows (green arrows, Figure S3C) that the limit cycle, if it exists in the model at the given parameter values, is always traversed clockwise. In other words, this means that, in the framework of the ADS+ model, the maximum of the total concentration of a GTPase (blue filled circle, Figure S3C) is always visited by the trajectory before the maximum of GTPase activity (red filled circle, FigureS3C). Furthermore, it is straightforward to see that when the limit cycle passes through the maximum of RT (red filled circle, Figure S3C), the time derivative of the total membrane RhoA is negative, $\dot{TR} < 0$. This simply follows from the fact that the maximum of RT lies always to the right of the nullcline (4) $\dot{TR} = 0$ on the phase plane (RT, TR) (Figure S3C). This provides a formal mathematical proof that in the ADS+ model the maximum of TR always precedes in time the maximum of RT. Importantly, this conclusion is independent of the specific values of the model parameters and is, thus, universal for the ADS+ model as defined by the model diagram in Figures 2B and S3A.

Analysis of the ADSI model

Following our earlier published work,[3,4] the three-variable ADSI model used here can be mathematically formulated as follows:

$$\begin{aligned}
\dot{RT} &= \left(k_0 + [GEF]\frac{k_1 RT^3}{1+k_2 RT^2}\right) RD - (k_3 + k_4[GAP]F)RT + d_{RT}\Delta RT \\
\dot{RD} &= -\left(k_0 + [GEF]\frac{k_1 RT^3}{1+k_2 RT^2}\right) RD + (k_3 + k_4[GAP]F)RT + k_5 - k_6 RD + d_{RD}\Delta RD, \\
\dot{F} &= k_7 + \frac{k_8 RT^2}{1+k_9 RT^2} - k_{10}F + d_F \Delta F
\end{aligned} \qquad \text{(Equation 7)}$$

where the numbering of constants follows Figure S3D and their representative values are given in Table S2. Rate k_{10}, not shown on Figure S3D, represents degradation of the inhibitor F (i.e., in molecular terms, depolymerization of F-actin). Here we also explicitly introduced the nondimensionalized concentrations of the positive feedback GEF and the negative feedback GAP to parametrize the strengths of positive and negative feedback, respectively. As in earlier analysis,[3,4] we assume that the model parameters are chosen so that the equations (7) have a single steady state whose stability changes with the variation of parameters that control the strength of positive and negative feedback, [GEF] and [GAP], respectively. Figure S3E shows a typical phase diagram of the model behavior on the plane of parameters [GEF] and [GAP]. Within the central triangular shaped domain of parameters, the steady state of the equations (7) is always unstable, and the model exhibits oscillatory waves. To the right of the oscillatory domain the model is excitable and can also exhibit waves. Importantly, linear stability analysis[4] shows that waves can be observed also to the left of the oscillatory domain, in the domain of the so-called wave instability,[58] also referred to sometimes as the finite wavelength Hopf, or the Turing-Hopf instability. Wave instability is a wave analogue of the stationary Turing instability that takes place when the homogeneous steady state loses stability via a pair of complex-conjugate eigenvalues and can be observed in models of (bio)chemical dynamics only with three or more variables. Therefore, the two-variable ADS and ADS+ models cannot possess the domains of parameters corresponding to the wave instability.

To predict the sign of time shift between the maxima of RT and TR we proceed as in the analysis of the ADS+ model above. Replacing RD by $TR - RT$ in (7) and omitting the diffusion terms, we obtain a system of three ordinary differential equations:

$$\begin{aligned}
\dot{RT} &= \left(k_0 + [GEF]\frac{k_1 RT^3}{1+k_2 RT^2}\right)(TR - RT) - (k_3 + k_4[GAP]F)RT \\
\dot{TR} &= k_5 - k_6(TR - RT) \\
\dot{F} &= k_7 + \frac{k_8 RT^2}{1+k_9 RT^2} - k_{10}F
\end{aligned} \qquad \text{(Equation 8)}$$

The nullclines of equations (8) are 2D surfaces in the 3D phase space and are not readily analyzable. Instead, we can reveal the sequence in which the oscillatory trajectory visits the maxima or RT and TR by projecting it onto the 2D plane (RT, TR) (Figure S3F). Note that unlike the oscillation trajectory of the ADS+ model (cf. Figure S3C), the direction of phase flow in the ADSI model is counterclockwise. Therefore, contrary to the dynamics of the ADS+ model (2), in the ADSI model (8) the maximum of RT always precedes that of TR in time. Again, this conclusion is independent of the exact values of model parameters and applies to waves in the oscillatory, excitable and wave instability domains of parameters (Figure S3E).

Current Biology, Volume *35*

Supplemental Information

Rho GTPase dynamics distinguish between models of cortical excitability

Dominic Chomchai, Marcin Leda, Adriana Golding, George von Dassow, William M. Bement, and Andrew B. Goryachev

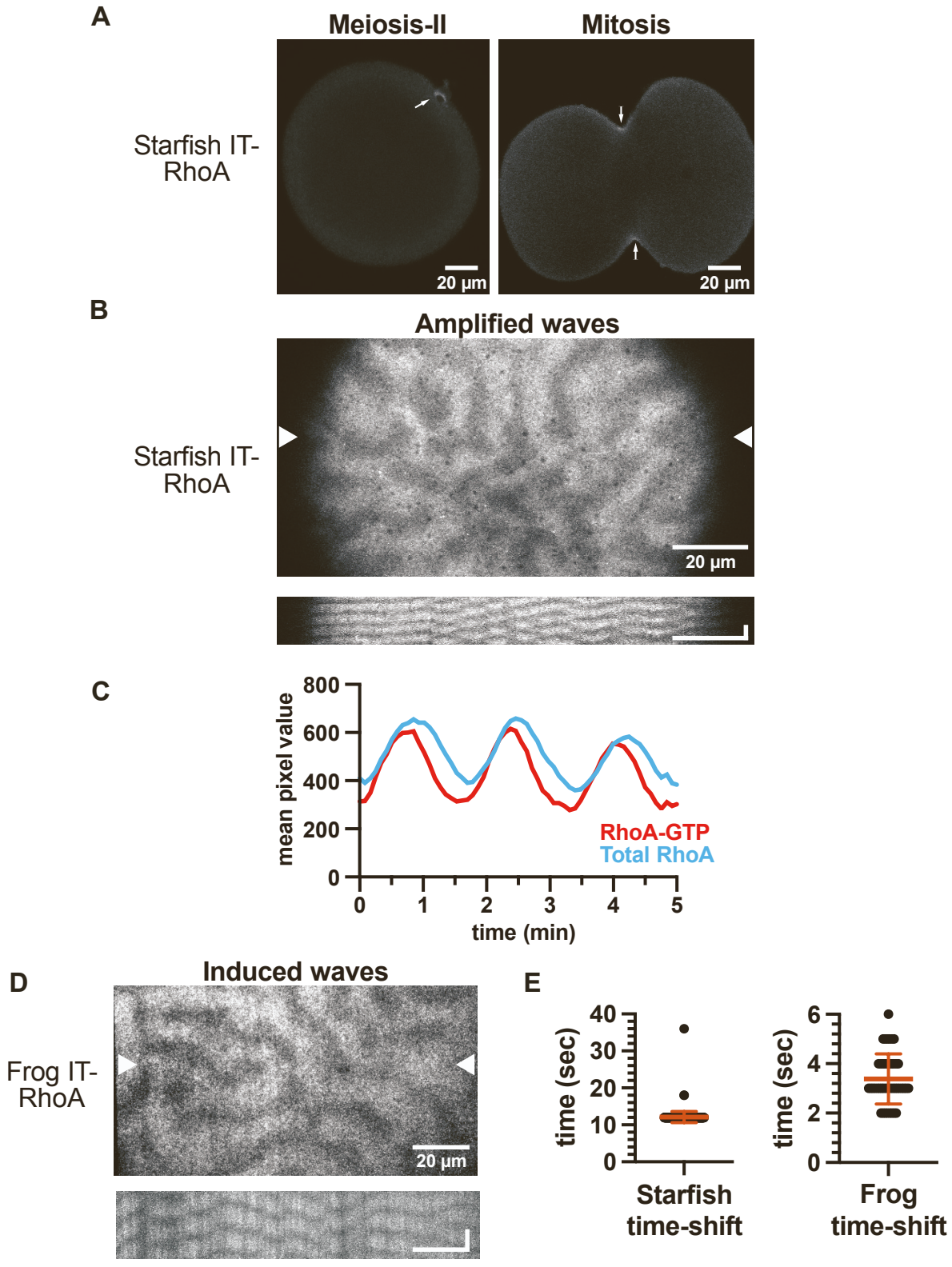
A
Meiosis-II
Mitosis
Starfish IT-RhoA
20 µm
20 µm
B
Amplified waves
Starfish IT-RhoA
20 µm
C
mean pixel value
800
600
400
200
0
0
1
2
3
4
5
time (min)
RhoA-GTP
Total RhoA
D
Induced waves
Frog IT-RhoA
20 µm
E
time (sec)
40
30
20
10
0
Starfish time-shift
time (sec)
6
4
2
0
Frog time-shift

Figure S1. IT-RhoA produces robust waves in starfish and frog oocytes. Related to Figure 1.

(A) Representative images of starfish oocytes exogenously expressing Ect2 shows IT-RhoA accumulation in polar body extrusion during Meiosis-II (left) and in the cortical furrow during mitosis (right). Arrows point to sites of IT-RhoA accumulation.

(B) Representative image and kymograph of a starfish oocyte exogenously expressing Ect2 produces robust, amplified waves of IT-RhoA.

(C) Representative wave profiles depicting the raw signals of RhoA-GTP (red) and IT-RhoA (cyan) extracted from a starfish oocyte exhibiting amplified cortical excitability.

(D) Representative image and kymograph of a frog immature oocyte exogenously overexpressing $Ect2^{dNLS}$ and RGA-3/4 displays distinct waves of IT-RhoA.

(E) Mean RhoA-GTP/Total RhoA time-shift of individual boxes in starfish oocyte *en face* movies (left, 12.12 ± 1.47 sec; ±SD; p-value <0.0001, two-tailed one-sample t-test) and frog immature oocyte medial section movies (right, 3.39 ± 1.01SD sec: ±SD; p-value <0.0001, two-tailed one-sample t-test) using an independent MATLAB script[16] (see methods). Each point represents the time-shift of an individual box.

Horizontal scale bars: 20 μm; Vertical scale bar: 2 min. Arrowheads indicate the location used for kymograph generation.

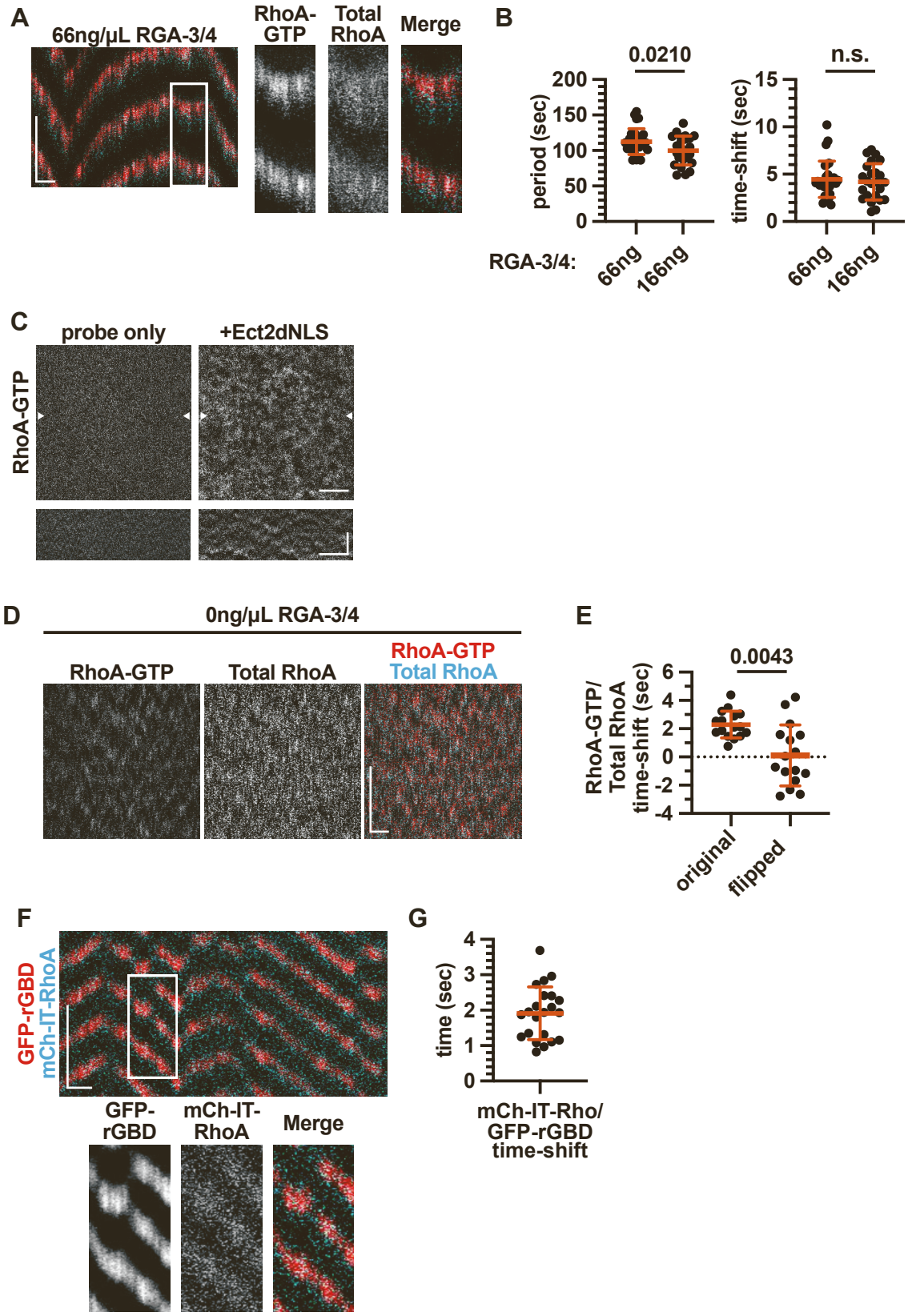
A
66ng/µL RGA-3/4
RhoA-GTP
Total RhoA
Merge
B
0.0210
n.s.
period (sec)
time-shift (sec)
RGA-3/4:
66ng
166ng
C
probe only
+Ect2dNLS
RhoA-GTP
D
0ng/µL RGA-3/4
RhoA-GTP
Total RhoA
RhoA-GTP
Total RhoA
E
0.0043
RhoA-GTP/
Total RhoA
time-shift (sec)
original
flipped
F
GFP-rGBD
mCh-IT-RhoA
GFP-
rGBD
mCh-IT-
RhoA
Merge
G
time (sec)
mCh-IT-Rho/
GFP-rGBD
time-shift

Figure S2. RhoA activity leads RhoA membrane enrichment in different wave regimes and with distinct fluorescent probes. Related to Figure 1.

(A) Representative kymograph of RhoA-GTP (red) and Total RhoA (cyan) waves from a medial section difference movie of a frog oocyte injected with 66 ng/μL needle concentration RGA-3/4, reduced compared to 166 ng/μL in Figures 1B-C.

(B) Left: Average wave period for the cellular conditions in A (66 ng/μL: 112.5 ± 18.10 SD sec; 166 ng/μL: 99.92 ± 20.40 SD sec; p-value: 0.0210; unpaired t-test). Right: Overall mean time shift between RhoA-GTP and Total RhoA signals for the conditions in A (66 ng/μL: 4.46 ± 1.91 SD sec; 166 ng/μL: 4.20 ± 1.92 SD sec; p-value: 0.3994; unpaired t-test).

(C) Representative still images of difference movies and corresponding kymographs of frog oocytes expressing no $Ect2^{dNLS}$ or RGA-3/4 (left) and $Ect2^{dNLS}$ without RGA-3/4 (right), showing pulse-like waves of RhoA-GTP.

(D) Representative kymographs of RhoA-GTP (red) and Total RhoA (cyan) waves from a medial section difference movie of frog immature oocytes expressing $Ect2^{dNLS}$ without RGA-3/4.

(E) Overall Mean time shift between RhoA-GTP and Total RhoA signals for the conditions in D. RhoA-GTP leads Total RhoA by 2.30 ± 0.94 SD sec. This time shift is abolished when the Total RhoA image is flipped vertically (0.11 ± 2.16 SD sec; p-value 0.0043, paired t-test).

(F) Representative kymographs from a medial section difference movie of RhoA-GTP (red) and Total RhoA (cyan) waves in frog immature oocytes expressing GFP-rGBD and mCh-IT-RhoA.

(G) Quantification for F showing that GFP-rGBD leads mCh-IT-RhoA by 1.91 ± 0.74 SD sec (p-value <0.0001; two-tailed one-sample t-test).

Horizontal scale bars: 10 μm; Vertical scale bar: 2 min. Arrowheads indicate the location used for kymograph generation. Each point in all dot plots represents the mean value for an individual cell.

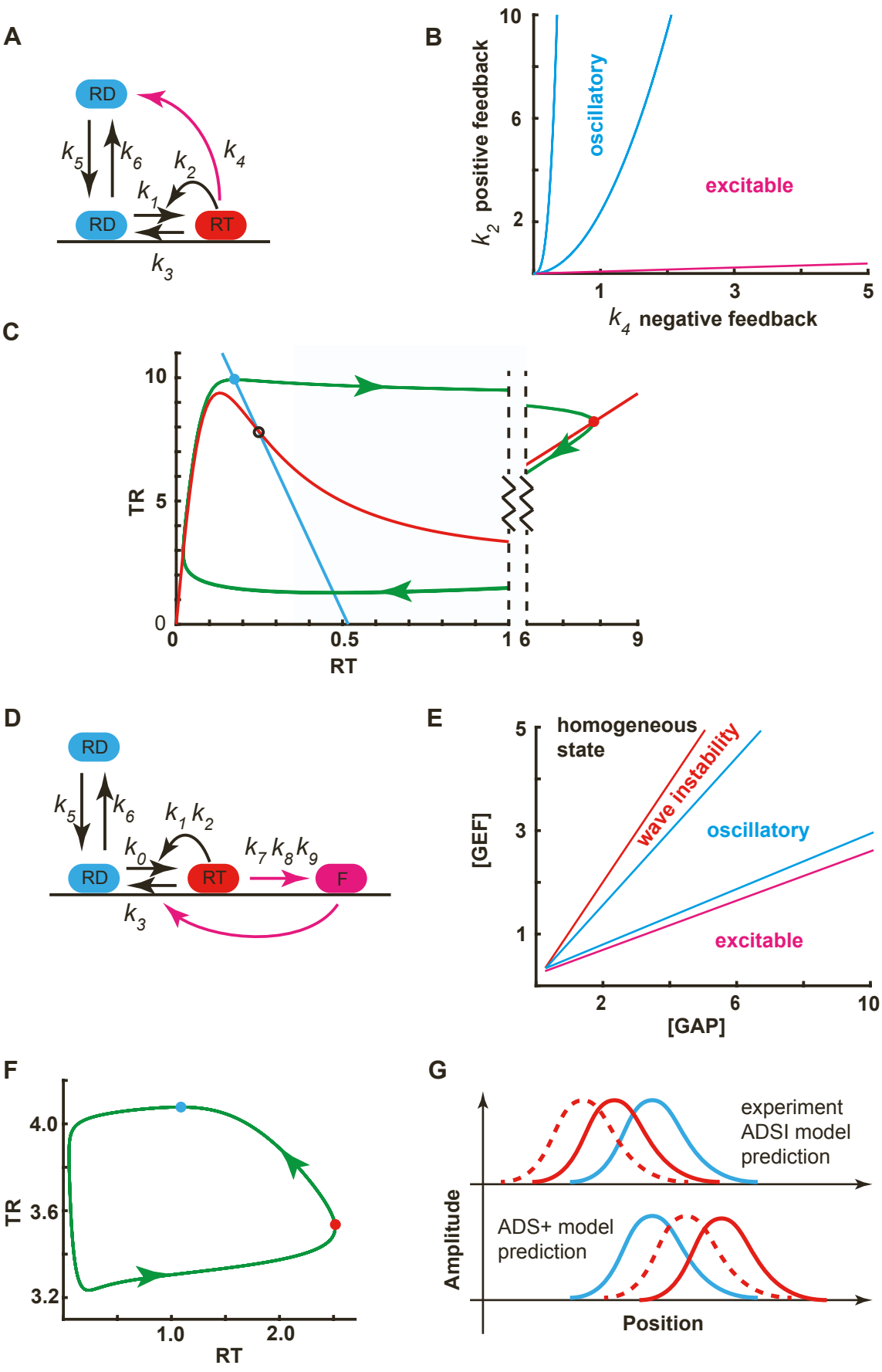
A
RD
RD
RT
k_1
k_2
k_3
k_4
k_5
k_6
B
10
6
2
k_2 positive feedback
oscillatory
excitable
1
3
5
k_4 negative feedback
C
10
5
0
TR
0
0.5
1
6
9
RT
D
RD
RD
RT
F
$k_1 k_2$
k_0
k_3
k_5
k_6
$k_7 k_8 k_9$
E
5
3
1
[GEF]
homogeneous state
wave instability
oscillatory
excitable
2
6
10
[GAP]
F
4.0
3.6
3.2
TR
1.0
2.0
RT
G
experiment
ADSI model prediction
ADS+ model prediction
Amplitude
Position

Figure S3. Mathematical analysis of the ADS+ and ADSI models. Related to Figure 2 and Tables S1 and S2.

(A) Reaction diagram of the ADS+ model with kinetic rate constants. See Table S1 for more details of kinetic rate constants.

(B) Sketch of the ADS+ model phase diagram.

(C) Phase portrait of the ADS+ model, with the phase flow direction indicated by a green line with arrows along the limit cycle.

(D) Reaction diagram of the ADSI model with kinetic rate constants. See Table S2 for more details of kinetic rate constants.

(E) Sketch of the ADSI model phase diagram.

(F) Projection of the 3D phase portrait of the ADSI model onto the plane (RT, TR). The green line with arrows represents the phase flow direction, while the red and cyan dots indicate the positions of the RT and TR maxima, respectively.

(G) Comparison of the model predictions and the experiment. IT-RhoA wave profile, cyan curve; signal of the activity reporter, solid red curve; true unknown profile of RhoA-GTP, red dash curve.

For detailed discussion of models and figure see STAR Methods.

k_1	0.001 s^{-1}
k_2	(0.05,0.45) $\mu M^{-2}s^{-1}$
k_3	0.01 s^{-1}
k_4	0.133333 s^{-1}
k_5	0.0666667 $\mu M*s^{-1}$
k_6	0.00444444 s^{-1}
d_{RT}	0.05 $\mu m^2/s$
d_{RD}	0.1 $\mu m^2/s$

Table S1 The ADS+ model parameters. Related to Figures 2 and S3.

k_0	0.00625 s^{-1}
k_1	0.3125 $\mu M^{-3}s^{-1}$
k_2	1 μM^{-2}
k_3	0.0625 s^{-1}
k_4	0.05625 $\mu M^{-1}s^{-1}$
k_5	0.0625 $\mu M*s^{-1}$
k_6	0.0208333 s^{-1}
k_7	0.001875 $\mu M*s^{-1}$
k_8	0.1406 $\mu M^{-1}s^{-1}$
k_9	0.25 μM^{-2}
k_{10}	0.025 s^{-1}
[GEF]	1.0
[GAP]	1.05
d_{RT}	0.08 $\mu m^2/s$
d_{RD}	0.4 $\mu m^2/s$
d_F	0 $\mu m^2/s$

Table S2 The ADSI model parameters. Related to Figures 2 and S3